

Accepted Article

Title: A Cysteine-Mediated Synthesis of Red Phosphorus Nanosheets

Authors: Jianbin Mo, Yun Xu, Longqian Zhu, Wei Wei, and Jing Zhao

This manuscript has been accepted after peer review and appears as an Accepted Article online prior to editing, proofing, and formal publication of the final Version of Record (VoR). This work is currently citable by using the Digital Object Identifier (DOI) given below. The VoR will be published online in Early View as soon as possible and may be different to this Accepted Article as a result of editing. Readers should obtain the VoR from the journal website shown below when it is published to ensure accuracy of information. The authors are responsible for the content of this Accepted Article.

To be cited as: *Angew. Chem. Int. Ed.* 10.1002/anie.202101486

Link to VoR: <https://doi.org/10.1002/anie.202101486>

A Cysteine-Mediated Synthesis of Red Phosphorus Nanosheets

Jianbin Mo^[a], Yun Xu^[b], Longqian Zhu^[b], Wei Wei^{*[a, b, c]} and Jing Zhao^{*[a, c]}

- [a] J. Mo, W. Wei, J. Zhao
State Key Laboratory of Coordination Chemistry, Chemistry and Biomedicine Innovation Center (ChemBIC), School of Chemistry and Chemical Engineering, Nanjing University, Nanjing, China
E-mail: Jingzhao@nju.edu.cn, weiwei@nju.edu.cn
- [b] Y. Xu, L. Zhu, W. Wei
School of Life Sciences, Nanjing University, Nanjing, China
- [c] W. Wei, J. Zhao
Shenzhen Research Institute, Nanjing University, Shenzhen, China

Supporting information for this article is given via a link at the end of the document.

Abstract: Among phosphorus-based nanomaterials, layered black phosphorus and violet phosphorus have been actively explored in the past decade. However, the synthesis of red phosphorus nanosheets (RPNSs) has been lacking although red phosphorus (RP) is commercially available at low cost and has excellent chemical stability at room temperature. Herein we report an efficient strategy to fabricate RPNSs and doped RPNSs using cysteine as a reducing reagent. Data from *in vitro* and *in vivo* studies suggested that RPNSs can trigger reactive oxygen species overexpression, DNA damage and subsequent autophagy-mediated cell death in a shape-dependent manner. Our findings not only provide a method to construct layered RP nanomaterials but also present a unique mechanism of phosphorus-based materials in nanomedicine.

Introduction

Phosphorus-based nanomaterials have recently been widely studied in energy, catalysis and nanomedicines^[1]. Black phosphorus (BP), a layered phosphorus-based material, has attracted much attention thanks to its unique physical and chemical characteristics^[2]. Yuan et al creatively designed a strategy to embed BP in matrix vesicles for bone regeneration^[2]. In particular, Yu et al elegantly demonstrated that black phosphorene could induce significant arrest of the G2/M phase in cancer cells, resulting in apoptosis and autophagy-mediated cell death^[3]. However, the exfoliation, characterization and application of BP need to be performed under protection, vastly restricting its further exploration^[4]. Among phosphorus allotropes, red phosphorus (RP) is abundant, commercially available at low cost, and environmentally friendly, and it has excellent chemical stability at room temperature, unlike violet, black and white phosphorus^[5]. Although RP has shown great potential in batteries as an anode material and in chemosynthesis as an electro/photocatalyst, its biological reactivity as a biomaterial has not been systematically explored. Furthermore, RP has been used mainly in nanospheres and irregular forms in different applications^[6]. The distinctive properties and possible applications of layered RP that can arise due to a free-standing structure have yet to be demonstrated. Therefore, developing a facile method for the synthesis of RP nanosheets (RPNSs) with

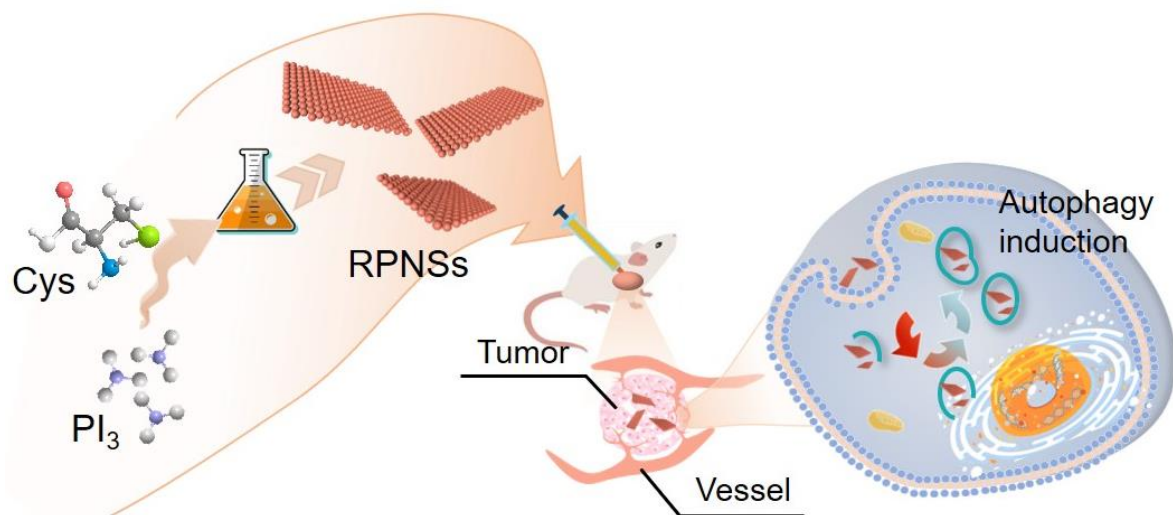
high quality and high yield will be particularly desirable for maximizing their chemical activity in potential biomedical applications.

Amino acids, as the basic building blocks of proteins, have special structures and fascinating active groups^[7]. A number of inspiring efforts have focused on using amino acids to construct nanomaterials. With the use of amino acids, different shapes of nanomaterials have been obtained and have shown outstanding capabilities in energy storage, catalysis and biomedicine^[8]. Early ingenious work by Kotov and his colleagues showed that cysteine could be used as a chiral stabilizer to generate ultrasmall CdTe nanocrystals and further induce unique structures^[9]. Pioneering studies by Kuang et al. revealed that phenylalanine could form covalent bonds between Cu²⁺ and oxygen atoms at the -COO-, while the aromatic group of phenylalanine provides a strong hydrophobic attraction for superparticle assembly^[10].

Herein we describe the synthesis of RPNSs by a free-standing solvent engineering route and report their anticancer properties. With detailed material characterization and systematic parameter control, we prepared a two-dimensional (2D) structure via a cysteine-directed redox reaction and grew it in 2D with the assistance of confinement substances. Cellular experiments revealed that DNA damage induced by RPNSs led to targeted autophagy in A549 lung cancer cells but not normal cells (Scheme 1). *In vivo* assessment confirmed the suppression of lung tumor growth, suggesting that RPNSs have immense potential in chemotherapy for lung cancer. Our results will help to design and fabricate phosphorus-based 2D nanomaterials from scratch and will provide guidance for broad applications of RP nanomaterials in nanomedicine.

Results and Discussion

RPNSs were generated via a typical redox reaction using phosphorus triiodide (PI₃) as the phosphorus source. To construct the 2D structure, L-cysteine (L-Cys) with weak reducibility was chosen as the reductant, CATB as the confinement substance, and PVP as the stabilizer. Our synthetic protocol is simple and involves two steps in a one-pot procedure.



Scheme 1. Summary diagram of the construction and therapeutic application of RPNSs. RPNSs were fabricated through a redox reaction between phosphorus triiodide and L-cysteine and acted as an autophagy accelerator to realize chemotherapy for cancer.

The first step was the redox reaction between PI₃ and Cys to gradually produce P atoms. Therefore, an aqueous Cys solution was added to initiate the reduction of PI₃. The ¹H NMR spectra of Cys showed that Cys was oxidized to cystine, indicating the successful occurrence of a redox reaction between PI₃ and Cys (Figure 1a). The detection of cystine (MW: 241) with LC-MS further indicated the oxidation of Cys (Figure 1b). PI₃ was first reduced by L-Cys, and then P atoms were released and assembled into nanostructures. The key step in this strategy is the introduction of an optimized amount of weak reductant, which can retard the 3D growth of RP with the assistance of CATB. The weakened reduction together with the confinement substances enabled a reaction equilibrium, and layered RPNSs were formed. Notably, this synthesis process should be maintained at room temperature to avoid degradation of PI₃ (Figure S1).

Analysis of the RPNSs with transmission electron microscopy (TEM) showed that the products were free-standing with a lateral size of 300 nm, which was consistent with dynamic light scattering (DLS) measurements (Figure 1c and 1d). A representative high-resolution TEM image and corresponding selected area electron diffraction pattern of RPNSs are shown in Figure 1e. These results revealed the disordered atomic structure and verified the amorphous characteristic of RPNSs. Interestingly, the translucent appearance and folded edges indicated the ultrathin nature of the RPNSs, which was further proven by height measurement with atomic force microscopy (AFM). As shown in Figure 1f and 1g, RPNSs are atomically flat, with a height of approximately 1.7 nm. The corresponding elemental mapping results showed uniform distributions of P and O in the nanosheets (Figure 1g). In addition, the homogeneity of RPNS ethanol/PBS dispersions with various concentrations from 0.05 to 0.2 mg/ml was evidenced by the existence of the Tyndall effect (Figure 1c and S1), indicating the good dispersibility of the RPNSs.

The crystal structure of the RPNSs was further investigated with X-ray diffraction (XRD). All the diffraction peaks could be indexed to RP because they were consistent with commercial RP (Figure 2a). Furthermore, the compositions were characterized through Raman spectroscopy. As shown in Figure 2b, the three prominent peaks could be attributed to the fundamental mode (B₁), symmetric stretch modes (A₁) and degenerate mode (E₁) of RP. Compared to commercial RP, the B₁, A₁ and E₁ modes of RPNSs are redshifted by approximately 9.5, 5.7 and 3.7 cm⁻¹, respectively. X-ray photoelectron spectroscopy was performed to study the surface properties of RPNSs and the chemical states of P (Figure 2c-2e). The P 2p spectrum showed three characteristic peaks at 129.9, 130.6 and 133.2 eV. The 2p_{3/2} and 2p_{1/2} of the P-P bond of P could be fitted to two peaks with binding energies of 129.9 and 130.6 eV. The weak peak at 133.2 eV was ascribed to the P-O bond, which might be formed through surface oxidation during air exposure. The oxidation of RPNSs was further determined by the existence of P=O and P-O bonds according to Fourier transform infrared spectroscopy (Figure 2f).

Compared with RPNSs prepared with L-Cys, RPNSs prepared with D-Cys also displayed a 2D nanosheet structure (Figure S3). When no cysteine was used in the synthesis process, an irregular nanostructure was obtained (Figure S4). Importantly, the use of CTAB as a confinement substance is the key factor in the formation of the layered structure (Figure S4). The natural tendency of RP toward 3D growth cannot be suppressed without enough CTAB. TEM images revealed that the presence of CTAB at concentrations of 0-30 μM led to the formation of sphere-shaped RP nanoparticles, and the use of CATB at concentrations above 40 μM produced 2D sheet-like nanomaterials (Figure S5).

A series of control experiments were carried out to demonstrate the specificity of Cys and CTAB in the fabrication of RPNSs. The morphologies of nanomaterials synthesized with

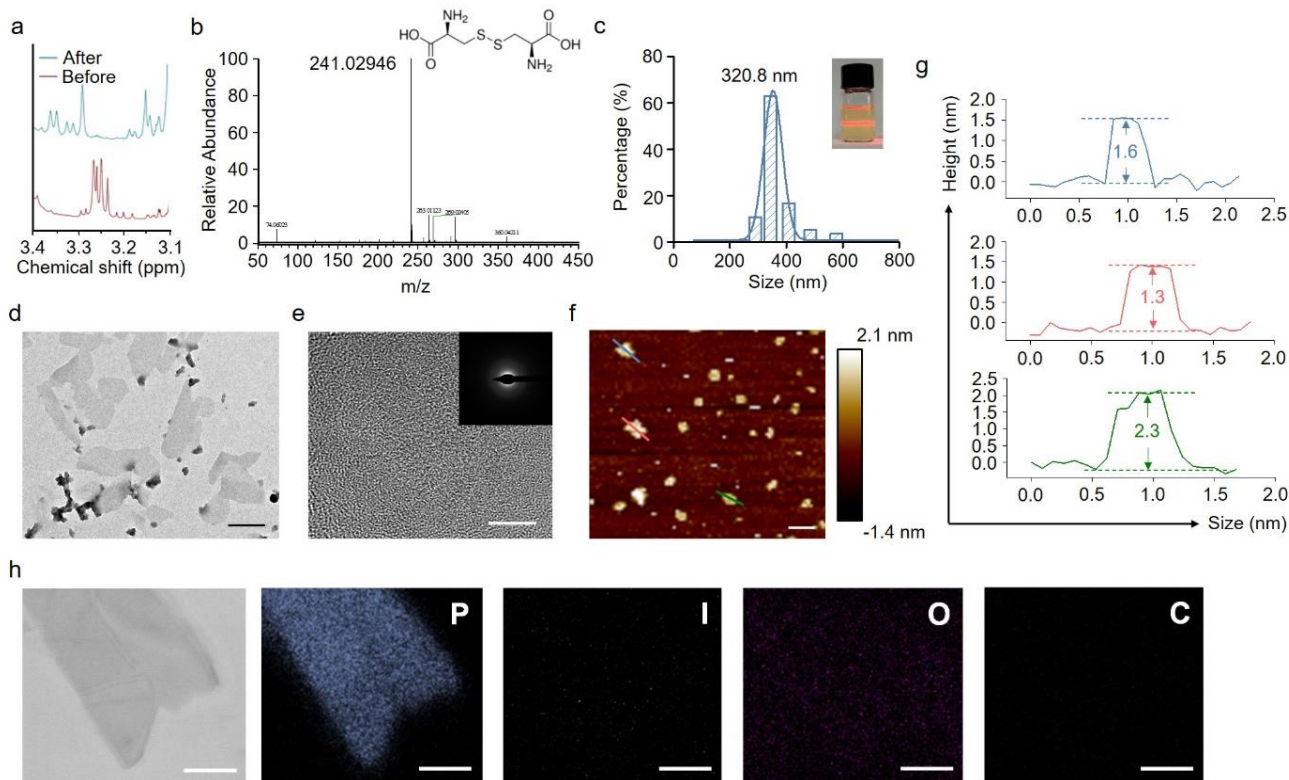


Figure 1. Morphology of the RPNSs. ^1H NMR spectra (a) and LC-MS analysis (b) of the reaction. (c) DLS analysis of RPNSs. The inset is a photograph of Tyndall effect of RPNSs solution. (d) TEM images of RPNSs. Scale bar: 200 nm. (e) High-resolution TEM image of the RPNSs with the inset displaying the SAED pattern. Scale bar: 5 nm. (f) AFM images of RPNSs. Scale bar: 500 nm. (g) Height profiles along the corresponding-colored lines in Figure 1f. (h) Element mapping analysis with EDS. Scale bar: 50 nm.

different reductants (vitamin C [VC] and sodium citrate [SC]) and confinement substances (methyl orange [MO]) and solvent (EthoH) are shown in TEM images (Figure S6). Specifically, RP nanospheres were produced in the presence of VC and SC, while an irregular nanostructure was synthesized in the other control experiments. All these RP nanostructures differed from the nanosheets prepared with cysteine, indicating that the Cys and CATB in this strategy played a critical role in forming the final 2D structures.

The evolution of the formation mechanism of RPNSs was further monitored (Figure S7). As Scheme 1 shows, RPNSs were constructed when PI_3 was reduced by L-Cys. The phosphorus atom was first released from PI_3 to assemble a small primary nanoparticle and then grew in 2D with the assistance of abundant CATB. The nanosheets reached their maximum lateral sizes after 4 h, and no obvious changes in their morphology occurred thereafter, even after 12 h. Notably, the P atom attached in an orderly manner to the RP primary cores within 30 min and then evolved into 2D RPNSs with the assistance of CATB.

Doping is a general and highly effective method to regulate the basic properties of nanomaterials for optoelectronics, catalysis and nanomedicine without changing the host crystal structure and fundamental characteristics^[11]. Here, we further attempted to construct metal atom-doped RPNSs through our simple synthesis strategy. Similar to the process of RPNSs fabrication, we added acetylacetonate to the reaction system.

Surprisingly, according to TEM results, a typical layered structure was obtained with the addition of iron(II) acetylacetonate or nickel(II) acetylacetonate (Figure 3a, S8 and S9). The AFM images in Figure 3b and 3c show that the average height of Fe(II)-doped RPNSs is 3.9 nm. The existence of Fe atoms in Fe(II)-doped RPNSs was confirmed through EDS mapping (Figure 3d and 3e). Notably, the layered doped RPNSs should be prepared with an appropriate atomic molar ratio. For example, the molar ratio of Fe(II) to P for constructing layered Fe(II)-doped RP was 1:5, while the layered structure could not be constructed with a ratio of 1:10 (Figure S8). However, the addition of cobalt(II) acetylacetonate and zinc(II) acetylacetonate produced irregular nanostructures (Figure S10 and S11). These results preliminarily revealed that our synthesis strategy would be a general method to obtain doped RPNSs with an appropriate atomic molar ratio. More and more studies have shown that metal nanoparticles, including Fe_3O_4 and Cu_xO , have multienzyme-like activities^[10, 12]. Inspired by these studies, we would like to explore the enzyme-like performances of metal atom-doped RPNSs, and the investigation of the properties and applications of doped RPNSs is still in progress.

To determine the bioactivity of RPNSs, we first investigated the biosafety of RPNSs. As shown in Figure S12, the hemolysis rates of RPNSs were less than 10% after 8 h of treatment, which confirmed the good hematological safety of the nanodrug. The cell viability of normal and cancer cell lines treated with RPNSs was determined by 1-[4,5-dimethylthiazol-2-yl]-2,5 diphenyl

tetrazolium bromide (MTT) assays (Figure 4a and S13). The RPNSs had high cytotoxicity toward cancer cells. After 24 h of incubation with 12.5 $\mu\text{g}/\text{ml}$ of RPNSs, the cell viability of 4T1, HeLa, A549, PL45 and U87 cells was only 34.1%, 41.8%, 38.9%, 45.3% and 48.7%, respectively. Notably, RPNSs possessed relatively low cytotoxicity toward several normal cell lines, including MC3T3-E1, HCM3 and 239T. After 24 h of treatment, the highest inhibition rate for 12.5 $\mu\text{g}/\text{ml}$ of RPNSs was 65.9%. Therefore, the RPNSs exhibited higher cytotoxicity to cancer cells than toward normal cells. Consistent with the MTT assay results, live/dead cell staining showed that a large number of A549 tumor cells were dead, while only hardly any normal human embryonic lung fibroblasts (HLF) were dead after treatment with 12.5 $\mu\text{g}/\text{ml}$ of RPNSs for 24 h (Figure S14). Importantly, the surface oxidation of RPNSs did not significantly affect the anticancer activity (Figure S15).

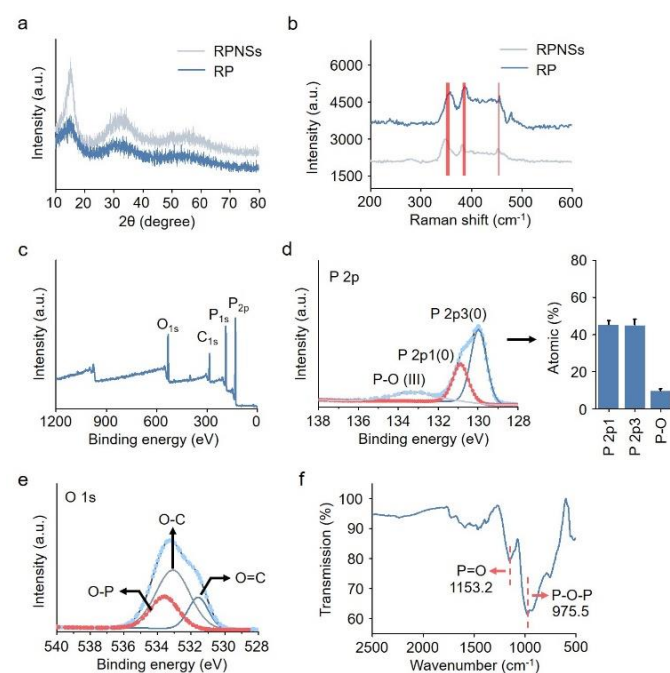


Figure 2. Structural characterization of the RPNSs. (a) XRD results of RPNSs and commercial RP. (b) Raman spectra of RPNSs. (c) XPS spectra acquired from the RPNSs. (d) High-resolution P 2p XPS spectrum. (e) High-resolution O 1s XPS spectrum. (f) Fourier transform infrared spectroscopy assay of RPNSs

We further investigated the cytotoxicity caused by RPNSs in terms of their special structure. The synthesized RPNSs have a planar structure, so a comparison was made with RP nanomaterials with different shapes and a bulk material. The shapes of RPNSs-VC and RPNSs-SC are shown in Figure S6, and their surface zeta potential was examined. The zeta potential of the RPNSs-Cys was -27.5 mV, while the zeta potentials of the RPNSs-VC and RPNSs-SC were -25.3 mV and -25.7 mV, respectively (Figure S16). Notably, the dispersibility of RP in aqueous solution is very low, which makes it difficult to obtain the precise zeta potential of RP. The efficient anticancer activity of RPNSs-Cys is shown in Figure S17, and no apparent growth inhibition was observed in the four cell lines. These

results indicated that the specific cytotoxicity caused by RPNSs was due to its layered nanostructure.

The mechanism of the cytotoxicity of RPNSs was then investigated. A lactate dehydrogenase (LDH) assay was first performed to study the interactions between RPNSs and the cell membrane. As shown in Figure S18, almost no LDH leakage was detected in cancer cells (A549) and normal cells (HLF) after treatment with RPNSs for 12 h or 24 h. This result reveals that RPNSs induce programmed cell death but not necrosis in cancer cells. Since apoptosis is one of the origins of cell death, the efficient induction of apoptotic and programmed cell death is considered the key factor in the clinical application of anticancer agents. Hence, an apoptotic study was carried out on RPNS-treated cells through fluorescence-activated cell sorting (FACS). Few early apoptotic cells (7.56% for 12.5 $\mu\text{g}/\text{ml}$ RPNS treatment) and hardly any late apoptotic cells (1.61% for 12.5 $\mu\text{g}/\text{ml}$ RPNS treatment) were detected, indicating a slight relationship between RPNSs and apoptosis induction in cancer cells (Figure S19). Besides, we also analyzed the apoptosis in different types of cancer cells (including U87, HeLa, 4T1 and PL45) through mitochondrial transmembrane potential and caspase 3/7 protein analysis (Figure S20-S26). These results showed no evident depolarization of the mitochondria and activation of caspase 3/7 in RPNSs-treated cells, indicating that RPNSs could only induce negligible apoptosis in cancer cells. In addition to apoptosis and necrosis, ferroptosis is recognized as a new cell death, which is iron-dependent and caused by the accumulation of oxidized phospholipids^[13]. Hence, we firstly detected the production of oxidized phospholipids in cancer cells using the lipid peroxidation-sensitive dye Bodipy-C11 (BODIPY).

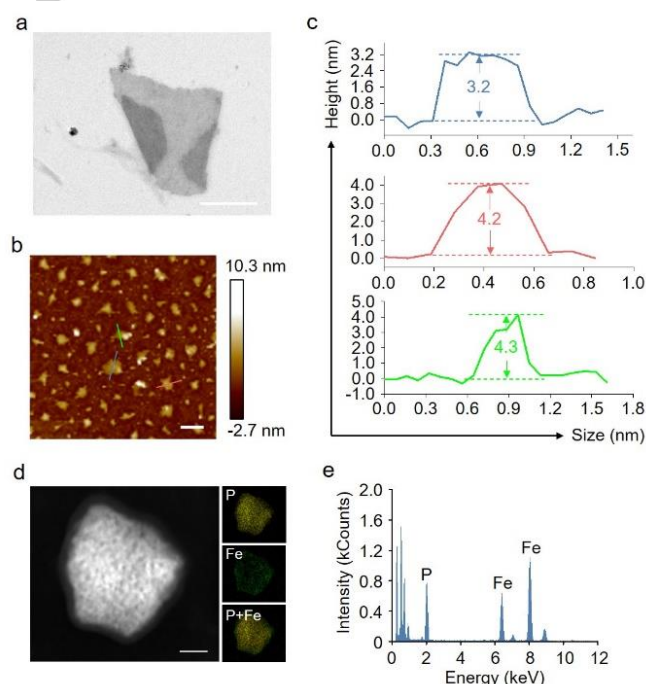


Figure 3. Construction of Fe(II)-doped RPNSs. (a) TEM images of Fe(II)-doped RPNSs. Scale bar: 500 nm. (b) AFM images of Fe(II)-doped RPNSs. Scale bar: 1 μm . (c) Height profiles along the corresponding colored lines in b. (d) STEM images of RPNSs. Scale bar: 20 nm. (e) EDS mapping analysis of RPNSs.

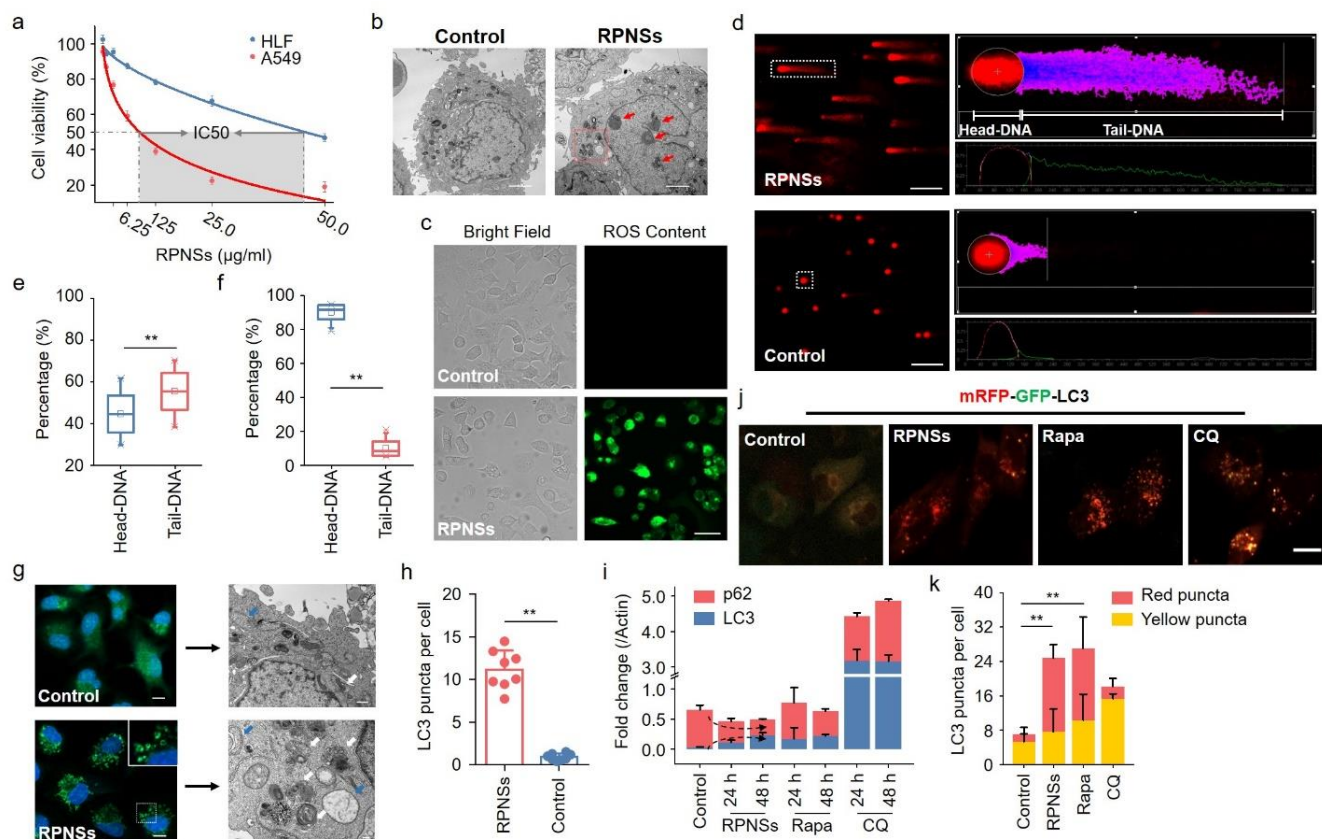


Figure 4. Cytotoxicity of the RPNSs. (a) Cell viability of A549 and HLF cells treated with 12.5, 6.25, 3.13 and 1.56 $\mu\text{g/ml}$ RPNSs for 24 h. (c) Bio-TEM images of RPNSs-treated A549 cells. Scale bar: 2 μm . (c) ROS staining in A549 cells before and after RPNSs treatments. Scale bar: 20 μm . (d) Single-cell gel electrophoresis analysis of A549 cells treated with 12.5 $\mu\text{g/ml}$ RPNSs for 24 h. Scale bar: 20 μm . (e-f) The statistics of percentages of head- and tail-DNA for (e) RPNSs-treated cells and (f) control cells in Figure 4d. (i) Immunofluorescence analysis of LC3 in RPNSs-treated cells and untreated cells (left). Scale bar: 20 μm . Bio-TEM images of RPNSs-treated cells and untreated cells (right). Scale bar: 200 nm. Typical structures of autophagosomes and autolysosomes are indicated with blue and white arrows, respectively. (h) Quantification of the number of LC3 puncta per cell in A549 cells. (i) Semiquantified analysis of LC3 and p63 proteins in RPNSs-treated cells and untreated cells. (j) Fluorescence images of autophagic flux with the mRFP-GFP-LC3 reporter. Autophagosomes fluoresce yellow (mRFP⁺/GFP⁺), and autolysosomes fluoresce red (mRFP⁺/GFP⁻). Scale bar: 20 μm . (k) Quantification of the number of red and yellow puncta per cell in A549 cells. All values are expressed as the mean \pm SD of triplicates. Statistical significance was assessed by Student's t test. * $p < 0.05$, ** $p < 0.01$.

As shown in Figure S27, BODIPY was readily oxidized when ferroptosis was elicited by RSL3 in cancer cells (including A549, U87 and HeLa), but no probe oxidation was detectable in cancer cells with RPNSs treatment. Then, the induction of ferroptosis by RPNSs was further determined by treating cancer cells with ferroptosis inhibitor ferrostatin-1 (Fer-1) or iron chelator deferoxamine (DFO). Fer-1 or DFO could block ferroptosis, but the RPNSs-induced cell death could not be significantly rescued by these inhibitors (Figure S28). Taken together, RPNSs could not induce evident apoptosis, necrosis or ferroptosis in cancer cells (including HeLa, U87, PL45, A549 and 4T1).

To further explore the mechanism of RPNSs in killing cancer cells, microcosmic morphological changes in RPNSs-treated cells were observed with TEM (Figure 4b). According to TEM images, condensed chromatin in the nucleus was observed (red arrow), which revealed that DNA damage was induced by RPNSs. Reactive oxygen species (ROS) are oxygen-containing molecules with reactivity for triggering oxidative stress, resulting in DNA damage. Therefore, the presence of ROS was determined by staining with cell-permeable fluorescent dye (dichlorofluorescein, DCF). Bright green fluorescence was

detected after RPNSs treatment in A549 cancer cells, while no obvious change in fluorescence strength was observed in normal cells after RPNSs-treatment (Figure 4c and S29). These results indicated that RPNSs induced the overexpression of ROS in cancer cells. The induction of DNA damage was further confirmed by single-cell gel electrophoresis (SCGE). As shown in Figure 4d, the RPNSs-treated cells exhibited a typical comet tail. Compared to nontreated cells, the percentage of DNA from RPNSs-treated cells in the comet tail increased from 9.8% to 55.4% (Figure 4e and 4f). On the other hand, RPNSs showed no genotoxicity to normal cells (Figure S30).

Importantly, through bio-TEM images, we found that typical autophagosomes and autolysosomes appeared in RPNSs-treated cells (Figure 4g and 4h). Autophagy is a self-degradative process that influences pivotal functions in regulating energy sources and excluding unnecessary metabolic products in the cell^[14]. Increasing evidence has demonstrated that autophagy is closely related to DNA damage^[15], and drastic autophagy leads to cell death^[16]. First, the induction of cell death by autophagy was verified by treating cancer cells with the autophagic inhibitor chloroquine (CQ). CQ treatment blocked autophagy in cancer

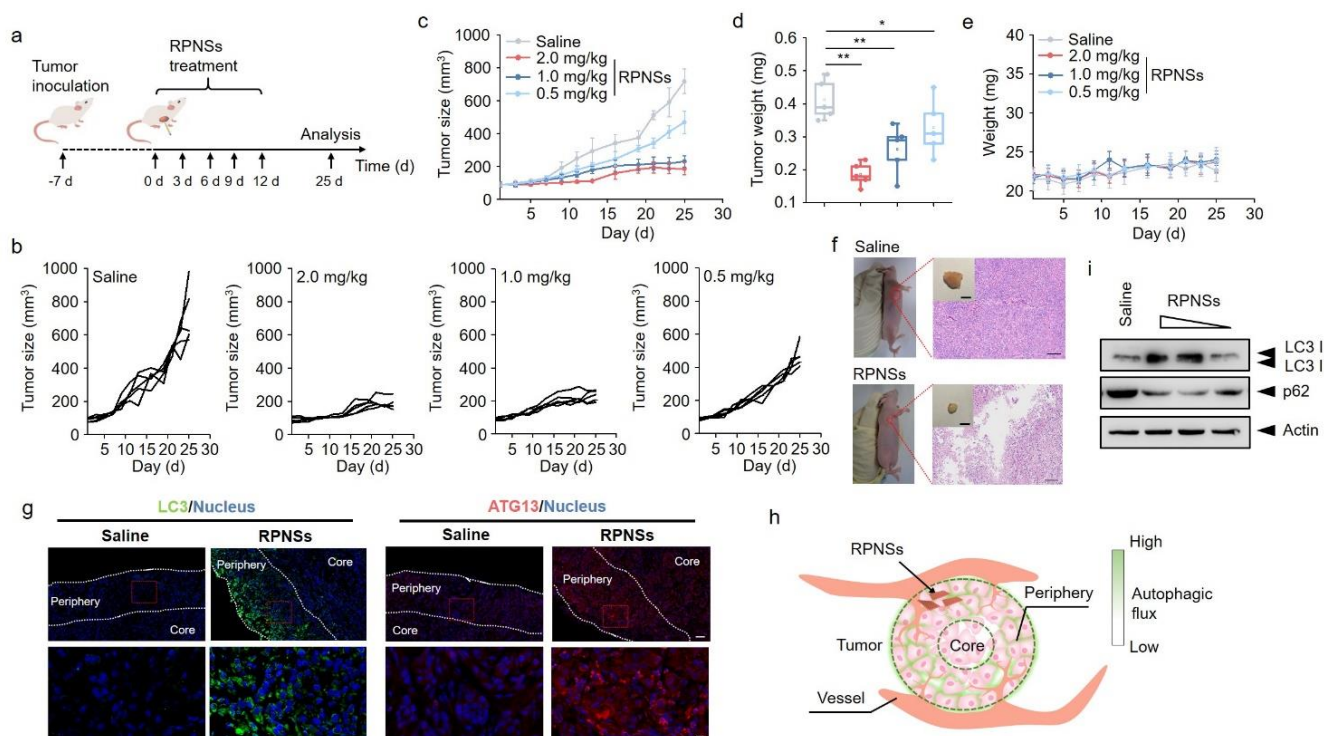


Figure 5. *In vivo* cancer chemotherapy with RPNSs. (a) Schematic illustration of the animal experimental design. (b) Tumor growth curves of individual mice in different groups of A549-bearing nude mice model. (c) The mean tumor growth curves of the mouse model under different treatments. (d) The mean weight of tumor tissues excised from the A549-bearing nude mouse model on day 25. (e) Body weight of mice during the treatment. (f) H&E staining of tumor tissues collected from mice on day 25 (inset: representative photographs of tumor tissues). Scale bar: 100 μ m (inset: 5 mm). (g) Immunostaining of LC3 and ATG13 in tumor tissues of control group and RPNSs (2.0 mg/kg)-treated mice. Scale bar: (up) 20 μ m and (down) 100 μ m. (h) Schematic view the obvious autophagic flux in the periphery of the tumor tissues. (i) Immunoblot analysis of the autophagy-related protein LC3 and p62 in tumor tissues from mice after treatment. Actin was set as the loading control. All values are expressed as the mean \pm SD of triplicates. Statistical significance was assessed by Student's t test. * p <0.05, ** p <0.01.

cells and reversed the cellular viability of RPNSs-treated cells from 38.9% to 72.4%, indicating an explicit relationship between autophagy and RPNSs (Figure S31). To further determine whether RPNSs induce autophagosome accumulation through decreased degradation or increased formation of autophagosomes, we examined the autophagy flux in RPNSs-treated cells with a series of independent assays. For all assays, cells treated with the autophagy inhibitor CQ were used as a negative control, while autophagy inducer (rapamycin, Rapa)-treated cells were used as a positive control. LC3 has been recognized as a significant marker for autophagy^[17]. After treatment with RPNSs for 24 h, the expression of LC3-I completely disappeared, and the lipidation of LC3 (LC3-II) was upregulated (Figure 4i and S32). Furthermore, p62, as a specific substrate, was obviously degraded in RPNSs-treated cells with enhanced autophagy flux. These results can be found in the positive control but not the negative control, indicating that RPNSs have the potential to promote autophagy. Then, RPNSs-induced autophagic flux was explored using a tandem fluorescent-tagged LC3 reporter (mRFP-GFP-LC3). The LC3 reporter initially fluoresces yellow (red merge green) as it labels autophagosomes, while it only shows red fluorescence after fusion with lysosomes to form autolysosomes^[18]. When treated with 12.5 μ g/ml RPNSs, the average red puncta per cell significantly increased from 2 to 17, consistent with the effect of an autophagy inducer (Figure 4j, 4k and S33). Finally, we

examined the key genes of autophagy in RPNSs-treated cells by quantitative real-time polymerase chain reaction (RT-PCR). The results showed that compared with untreated cancer cells, the mRNA levels of autophagy-related key genes (including ULK-1, ATG13, LC3, NANOG, SOX2, and POU5F1) increased in A549 cells after treatment with RPNSs (Figure S34). For further verified bioactivity of RPNSs in promoting autophagy, we expanded the detection of autophagy in other types of cancer cells. Through immunofluorescence analysis of LC3 and RT-PCR, we found RPNSs could induce obvious autophagy in not only A549 cells but also other cancer cells including Hela, PL45, U87 and 4T1 (Figure S34 and S35).

After demonstrating the anticancer effects of RPNSs and their ability to induce autophagy *in vitro*, the tumor suppression effects were systematically determined in A549-bearing nude mice. The mice were randomly divided into four groups and intravenously injected with saline (control group) and different concentrations of RPNSs (2, 1 and 0.5 mg/kg) five times every three days (Figure 5a). Tumor growth was significantly hindered in a concentration-dependent manner after RPNSs injection (Figure 5b). As expected, after RPNSs treatment, the tumor volume slightly increased from 90.3 mm³ to 183 mm³, while that of the tumor in the control group significantly increased from 89.26 mm³ to 718.1 mm³ (Figure 5c). The mean weights of tumor tissues from the control group and RPNS-treated group were 0.41 mg and 0.19 mg, respectively, indicating that the

tumor growth inhibition value was 53.7% (Figure 5d). During the treatment, the mice in the RPNS-treated group had body weights comparable to those in the control group (Figure 5e). Hematology, blood biochemistry and histological analysis further revealed that RPNSs induced no evident toxic side effects at an effective dose (Figure S36-S38). According to H&E staining of the excised tumor tissues, more efficient cancer cell shrinkage and tissue necrosis were observed in the mice injected with RPNSs than in the saline-treated mice (Figure 5f). To determine the molecular mechanism *in vivo*, two independent assays were performed. We conducted immunostaining of LC3II and ATG13 in tumor-bearing mice, two key biomarkers of autophagic flux in tumors. As shown in Figure 5g, obvious LC3II and ATG13 puncta accumulated in the tumor tissue from RPNSs-treated mice. Notably, autophagic flux was evident in the periphery and around the blood vascular network (Figure 5g and 5h). Western blot analysis further confirmed that RPNSs effectively induced autophagy in a concentration-dependent manner (Figure 5i). The above results suggested that RPNSs with excellent biocompatibility displayed a superior therapeutic effect for cancer.

Conclusion

In summary, we have established that amorphous RPNSs could be constructed through a redox reaction-based strategy. In this strategy, L-Cys was used as a key reductant to promote RPNSs assembly, while CATB acted as a confinement substance to ensure 2D growth. The addition of metal ions to the reaction system can enable the fabrication of metal atom-doped RPNSs with potential new properties, which further broadens the application of this strategy. For example, since Fe^{2+} is an accepted catalyst in peroxide decomposition, we speculated that Fe(II)-doped RPNSs could be used as peroxidase-mimicking nanozymes for nanomedicine. With high surface activity, native RPNSs selectively induce ROS overexpression, resulting in drastic oxidative stress and DNA damage in A549 lung cancer cells. Intriguingly, our findings revealed that RPNSs can obviously enhance autophagy by promoting the fusion of autophagosomes and lysosomes, which is a different anticancer mechanism from that of black phosphorus^[9]. According to *in vivo* chemotherapy, RPNSs were demonstrated to be an autophagy inducer and a promising agent without toxic side effects for lung cancer therapy. The current work may not only illuminate the important roles of RPNSs in biomedicine but also open a new avenue for phosphorus-based nanomaterials.

Acknowledgements

Financial support was provided by the National Natural Science Foundation of China (21671099 and 91753121), and the Shenzhen Basic Research Program

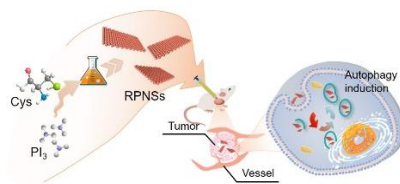
(JCYJ20180508182240106), supported by the Fundamental Research Funds for the Central Universities (020514380139).

Keywords: red phosphorus nanosheets • cysteine • autophagy • chemotherapy

- [1] a)Y. Zhang, X. Rui, Y. Tang, Y. Liu, J. Wei, S. Chen, W. R. Leow, W. Li, Y. Liu, J. Deng, B. Ma, Q. Yan, X. Chen, *Adv. Energy Mater.* **2016**, *6*, 1502409; b)B. Liu, Q. Zhang, L. Li, Z. Jin, C. Wang, L. Zhang, Z.-M. Su, *ACS Nano* **2019**, *13*, 13513-13523; c)C. Qi, S. Musetti, L.-H. Fu, Y.-J. Zhu, L. Huang, *Chem. Soc. Rev.* **2019**, *48*, 2698-2737; d)Y. Zhu, C. Lv, Z. Yin, J. Ren, X. Yang, C.-L. Dong, H. Liu, R. Cai, Y.-C. Huang, W. Theis, S. Shen, D. Yang, *Angew. Chem. Int. Ed.* **2020**, *59*, 868-873.
- [2] a)W. Chen, J. Ouyang, H. Liu, M. Chen, K. Zeng, J. Sheng, Z. Liu, Y. Han, L. Wang, J. Li, *Adv. Mater.* **2016**, *29*; b)R. Gusmão, Z. Sofer, M. Pumera, *Angew. Chem. Int. Ed.* **2017**, *56*, 8052-8072; c)W. Hui, Y. Xianzhu, S. Wei, C. Shichuan, X. Junfeng, Z. Xiaodong, W. Jun, X. Yi, *J. Am. Chem. Soc.* **2015**, *137*, 11376-11382; d)J. Mo, Y. Xu, X. Wang, W. Wei, J. Zhao, *Nanoscale* **2020**, *12*, 1742-1748; e)L. Li, Y. Yu, G. J. Ye, Q. Ge, X. Ou, H. Wu, D. Feng, X. H. Chen, Y. Zhang, *Nat. Nanotechnol.* **2014**, *9*, 372-377; f)Y. Wang, X. Hu, L. Zhang, C. Zhu, J. Wang, Y. Li, Y. Wang, C. Wang, Y. Zhang, Q. Yuan, *Nat. Commun.* **2019**, *10*, 2829; g)L. Liang, Y. Tang, X. Hu, J. Wang, S. Xiao, D. Li, L. Fu, Z. Li, Q. Yuan, *CCS Chemistry*, *1*, 490-501.
- [3] W. Zhou, T. Pan, H. Cui, Z. Zhao, P. K. Chu, X.-F. Yu, *Angew. Chem. Int. Ed.* **2019**, *58*, 769-774.
- [4] P. E. M. Amaral, G. P. Nieman, G. R. Schwenk, H. Jing, R. Zhang, E. B. Cerkez, D. Strongin, H.-F. Ji, *Angew. Chem. Int. Ed.* **2019**, *58*, 6766-6771.
- [5] S. A. Ansari, Z. Khan, M. O. Ansari, M. H. Cho, *RSC Adv.* **2016**, *6*, 44616-44629.
- [6] a)J. Zhou, X. Liu, W. Cai, Y. Zhu, J. Liang, K. Zhang, Y. Lan, Z. Jiang, G. Wang, Y. Qian, *Adv. Mater.* **2017**, *29*, 1700214; b)W. Liu, S. Ju, X. Yu, *ACS Nano* **2020**, *14*, 974-984; c)S. Liu, H. Xu, X. Bian, J. Feng, J. Liu, Y. Yang, C. Yuan, Y. An, R. Fan, L. Ci, *ACS Nano* **2018**, *12*, 7380-7387.
- [7] a)M. Mravic, J. L. Thomaston, M. Tucker, P. E. Solomon, L. Liu, W. F. DeGrado, *Science* **2019**, *363*, 1418-1423; b)R. A. Harte, J. J. Travers, *Science* **1947**, *105*, 15-16.
- [8] a)X. Gao, X. Zhang, K. Deng, B. Han, L. Zhao, M. Wu, L. Shi, J. Lv, Z. Tang, *J. Am. Chem. Soc.* **2017**, *139*, 8734-8739; b)R. Malishev, E. Arad, S. K. Bhunia, S. Shaham-Niv, S. Kolusheva, E. Gazit, R. Jelinek, *Chem. Commun.* **2018**, *54*, 7762-7765; c)B. Ma, S. Wang, F. Liu, S. Zhang, J. Duan, Z. Li, Y.

- Kong, Y. Sang, H. Liu, W. Bu, L. Li, *J. Am. Chem. Soc.* **2019**, *141*, 849-857.
- [9] Y. Zhou, M. Yang, K. Sun, Z. Tang, N. A. Kotov, *J. Am. Chem. Soc.* **2010**, *132*, 6006-6013.
- [10] C. Hao, A. Qu, L. Xu, M. Sun, H. Zhang, C. Xu, H. Kuang, *J. Am. Chem. Soc.* **2019**, *141*, 1091-1099.
- [11] a)C.-G. Liu, Y.-H. Han, J.-T. Zhang, R. K. Kankala, S.-B. Wang, A.-Z. Chen, *Chem. Eng. J.* **2019**, *370*, 1188-1199; b)P. Błoński, J. Tuček, Z. Sofer, V. Mazánek, M. Petr, M. Pumera, M. Otyepka, R. Zbořil, *J. Am. Chem. Soc.* **2017**, *139*, 3171-3180; c)J. Kim, S. S. Baik, S. H. Ryu, Y. Sohn, S. Park, B.-G. Park, J. Denlinger, Y. Yi, H. J. Choi, K. S. Kim, *Science* **2015**, *349*, 723-726.
- [12] L. Gao, J. Zhuang, L. Nie, J. Zhang, Y. Zhang, N. Gu, T. Wang, J. Feng, D. Yang, S. Perrett, X. Yan, *Nat. Nanotechnol.* **2007**, *2*, 577-583.
- [13] a)X. Jiang, B. R. Stockwell, M. Conrad, *Nat. Rev. Mol. Cell Biol.* **2021**; b)X. Chen, R. Kang, G. Kroemer, D. Tang, *Nat. Rev. Clin. Oncol.* **2021**.
- [14] a)B. Levine, G. Kroemer, *Cell* **2019**, *176*, 11-42; b)B. Levine, G. Kroemer, *Cell* **2008**, *132*, 27-42; c)Z. Zhong, E. Sanchez-Lopez, M. Karin, *Cell* **2016**, *166*, 288-298.
- [15] a)Y. Chen, J. Wu, G. Liang, G. Geng, F. Zhao, P. Yin, S. Newshean, C. Wu, Y. Li, L. Li, W. Kim, Q. Zhou, J. Huang, J. Liu, C. Zhang, G. Guo, M. Deng, X. Tu, X. Gao, Z. Liu, Y. Chen, Z. Lou, K. Luo, J. Yuan, *Sci. Adv.* **2020**, *6*, eaax5819; b)T. Robert, F. Vanoli, I. Chiolo, G. Shubassi, K. A. Bernstein, R. Rothstein, O. A. Botrugno, D. Parazzoli, A. Oldani, S. Minucci, M. Foiani, *Nature* **2011**, *471*, 74-79; c)S. Torii, H. Yamaguchi, A. Nakanishi, S. Arakawa, S. Honda, K. Moriwaki, H. Nakano, S. Shimizu, *Nat. Commun.* **2020**, *11*, 1754.
- [16] a)H. Li, Y. Li, J. Jiao, H.-M. Hu, *Nat. Nanotechnol.* **2011**, *6*, 645-650; b)S. J. Hawkins, L. A. Crompton, A. Sood, M. Saunders, N. T. Boyle, A. Buckley, A. M. Minogue, S. F. McComish, N. Jiménez-Moreno, O. Cordero-Llana, P. Stathakos, C. E. Gilmore, S. Kelly, J. D. Lane, C. P. Case, M. A. Caldwell, *Nat. Nanotechnol.* **2018**, *13*, 427-433; c)J. Tian, X. Zeng, X. Xie, S. Han, O.-W. Liew, Y.-T. Chen, L. Wang, X. Liu, *J. Am. Chem. Soc.* **2015**, *137*, 6550-6558.
- [17] A. M. Leidal, H. H. Huang, T. Marsh, T. Solvik, D. Zhang, J. Ye, F. Kai, J. Goldsmith, J. Y. Liu, Y.-H. Huang, T. Monkkonen, A. Vlahakis, E. J. Huang, H. Goodarzi, L. Yu, A. P. Wiita, J. Debnath, *Nat. Cell Biol.* **2020**, *22*, 187-199.
- [18] a)Z. Cui, Y. Zhang, K. Xia, Q. Yan, H. Kong, J. Zhang, X. Zuo, J. Shi, L. Wang, Y. Zhu, C. Fan, *Nat. Commun.* **2018**, *9*, 4347; b)J. Cai, R. Li, X. Xu, L. Zhang, R. Lian, L. Fang, Y. Huang, X. Feng, X. Liu, X. Li, X. Zhu, H. Zhang, J. Wu, M. Zeng, E. Song, Y. He, Y. Yin, J. Li, M. Li, *Nat. Cell Biol.* **2018**, *20*, 465-478.

Entry for the Table of Contents



In this work, we established a redox method for fabrication of RPNSs. Cysteine was found to be responsible for RPNSs assembly. Notably, the addition of acetylacetonate could enable the construction of doped RPNSs, which might further broaden the applications of RPNSs. In addition, our *in vitro* and *in vivo* results confirmed that native RPNSs induced drastic autophagy in the tumor chemotherapy.